

UC Irvine

UC Irvine Previously Published Works

Title

Octopus-inspired deception and signaling systems from an exceptionally-stable acene variant.

Permalink

<https://escholarship.org/uc/item/1590v1j2>

Journal

Nature Communications, 14(1)

Authors

Pratakshya, Preeta

Xu, Chengyi

Dibble, David

et al.

Publication Date

2023-12-22

DOI

10.1038/s41467-023-40163-7

Peer reviewed



Octopus-inspired deception and signaling systems from an exceptionally-stable acene variant

Received: 24 August 2022

Accepted: 14 July 2023

Published online: 22 December 2023

Check for updates

Preetta Pratakshya^{1,8}, Chengyi Xu^{2,8}, David J. Dibble^{3,8}, Aliya Mukazhanova^{1,4}, Panyiming Liu^{1,2}, Anthony M. Burke³, Reina Kurakake², Robert Lopez², Philip R. Dennison¹, Sahar Sharifzadeh^{1,4,5,6,7} & Alon A. Gorodetsky^{1,2,3}

Multifunctional platforms that can dynamically modulate their color and appearance have attracted attention for applications as varied as displays, signaling, camouflage, anti-counterfeiting, sensing, biomedical imaging, energy conservation, and robotics. Within this context, the development of camouflage systems with tunable spectroscopic and fluorescent properties that span the ultraviolet, visible, and near-infrared spectral regions has remained exceedingly challenging because of frequently competing materials and device design requirements. Herein, we draw inspiration from the unique blue rings of the *Haplochlaena lunulata* octopus for the development of deception and signaling systems that resolve these critical challenges. As the active material, our actuator-type systems incorporate a readily-prepared and easily-processable nonacene-like molecule with an ambient-atmosphere stability that exceeds the state-of-the-art for comparable acenes by orders of magnitude. Devices from this active material feature a powerful and unique combination of advantages, including straightforward benchtop fabrication, competitive baseline performance metrics, robustness during cycling with the capacity for autonomous self-repair, and multiple dynamic multispectral operating modes. When considered together, the described exciting discoveries point to new scientific and technological opportunities in the areas of functional organic materials, reconfigurable soft actuators, and adaptive photonic systems.

Multifunctional platforms that can adaptively modulate their color and appearance have attracted widespread attention for applications in displays, signaling, camouflage, anti-counterfeiting, sensing, biomedical imaging, energy conservation, and robotics^{1–21}. Such technologically valuable platforms typically exhibit dynamic spectroscopic properties that emerge from programming of their constituent materials for responsiveness to specific external stimuli (e.g.,

mechanical, electrical, magnetic, chemical, or thermal inputs)^{1–21}. Within this context, the development of systems with tunable spectroscopic and fluorescent properties that span the ultraviolet, visible, and near-infrared (UV–Vis–NIR) regions of the electromagnetic spectrum has proven challenging, especially for notoriously demanding tandem deception and signaling applications^{1–11}. Indeed, relatively few classes of camouflage systems with the potential for achieving such

¹Department of Chemistry, University of California, Irvine, Irvine CA 92697, USA. ²Department of Materials Science and Engineering, University of California, Irvine, Irvine, CA 92697, USA. ³Department of Chemical and Biomolecular Engineering, University of California, Irvine, Irvine, CA 92697, USA. ⁴Division of Materials Science and Engineering, Boston University, Boston, MA 02215, USA. ⁵Department of Chemistry, Boston University, Boston, MA 02215, USA.

⁶Department of Physics, Boston University, Boston, MA 02215, USA. ⁷Department of Electrical and Computer Engineering, Boston University, Boston, MA 02215, USA. ⁸These authors contributed equally: Preetta Pratakshya, Chengyi Xu, David J. Dibble. e-mail: alon.gorodetsky@uci.edu

desirable capabilities have been explored to date, including dual-band electrochromic devices, metamaterials/metasurfaces, electroactive polymers, reconfigurable photonic gels, and biomolecular films^{1–11,22–30}. Despite much recent progress, these systems have all consistently struggled with multiple critical drawbacks, such as complex constituent active material preparation methodologies, sophisticated and expensive clean room fabrication schemes, difficult incorporation of more than one tunable spectroscopic capability, a lack of functionality across multiple spectral bands, the requirement for a single type of actuation strategy, slow switching and response times, degradation or inconsistent performance upon repeated actuation, and/or the inability to autonomously self-repair during operation without user intervention^{1–11,22–30}. As such, there has emerged an exciting opportunity and powerful incentive for the development of multifunctional platforms that overcome the limitations of the reported technologies.

Within the realm of multifunctional deception and signaling platforms, one well-known class of active materials that has received comparatively minimal attention is acenes, which are organic polycyclic aromatic hydrocarbons consisting of linearly fused benzene rings and containing one aromatic sextet^{31–50}. This relative lack of attention is surprising because acenes exhibit a variety of advantageous attributes, which include straightforward synthetic accessibility, chemically modular pi-conjugated core structures, amenability to peripheral substitution and functionalization, compatibility with bench-top fabrication and processing procedures, theoretically well-understood electronic characteristics, and stimuli-responsive spectroscopic properties^{31–50}. Historically, the shorter acenes and heteroacenes (e.g., pentacene and its variants) have played pivotal roles in (1) organic chemistry as model polycyclic aromatic hydrocarbons (over the past ~70 years)^{31–33,37,38} and (2) organic optoelectronics as prototypical active materials for light-emitting diodes, solar cells, and field-effect transistors (over the past ~30 years)^{42,43,50}. More recently, significant research effort has been expended on obtaining and characterizing longer acenes (and, in particular, nonacene derivatives) because of their significance from a fundamental physical organic chemistry viewpoint and their theoretically predicted superior properties

for optoelectronic applications (e.g., smaller band gaps, higher mobilities, and tunable visible to near-infrared spectra)^{33–36,39–41,44,48,51–61}. However, the solution-based synthesis of classic nonacene or its variants has been reported in a handful of studies (only 7 total), with these compounds featuring insufficient solid-state stabilities of at most two months even under inert conditions, qualitatively evaluated poor solution-phase stabilities of seconds to hours in ambient atmosphere under light, and limited solubilities in multiple kinds of solvent systems (Supplementary Table 1)^{51–57}. Consequently, the previously studied nonacene variants could neither be processed into thin films nor used in conventional fabrication schemes and their utility for device applications was never explored (Supplementary Table 1)^{51–61}, therefore leaving these molecules' technological potential largely unknown.

Herein, we report bioinspired deception and signaling systems, which use a designer nonacene-like molecule with exceptional stability as the active material and thus demonstrate a unique combination of powerful capabilities. For the conceptualization of such systems, we examine the dynamic camouflage and aposematic warning display abilities of *Hapalochlaena lunulata* (*H. lunulata*) octopus skin (Fig. 1A), which are enabled by the muscle-controlled switching of iridescent blue rings between hidden and exposed states on a contrast-enhancing brown background (Fig. 1B)⁶². Moreover, we draw upon the literature precedent reported for the synthesis of nonacene derivatives^{51–57} and nitrogen-containing tetrabenzopentacenes^{63,64}, as well as upon the technical foundation previously established in our studies of adaptive infrared camouflage systems^{65–67}. Consequently, we envision blue ring-type dielectric elastomer actuator (DEA) devices consisting of a top transparent proton-conducting polymer electrode, a nonacene variant-based active layer wherein a wrinkled blue annulus surrounds a flatter brown circle, an underlying acrylic dielectric elastomer membrane, and a bottom transparent proton-conducting polymer electrode (Fig. 1C). Before actuation, we anticipate that such devices will feature contracted microstructured active regions with bright visible appearances, strong associated near-infrared signatures, and large corresponding fluorescence signals (Fig. 1C, left), but after actuation, we anticipate that such devices will feature expanded

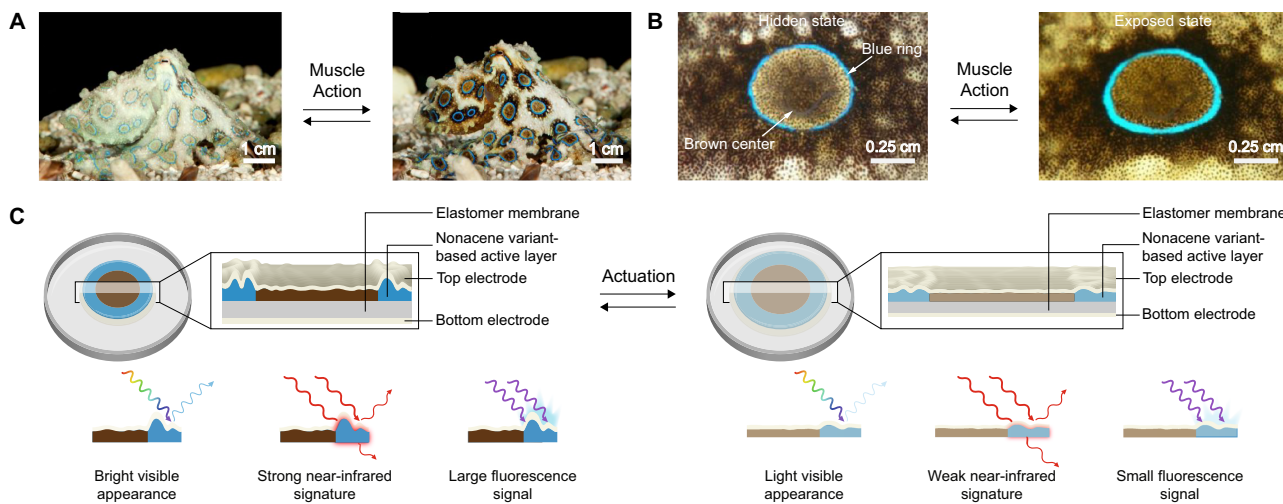


Fig. 1 | The blue-ringed octopus as biological inspiration and the conceptualization of deception and signaling systems. **A** Pictures of the *H. lunulata* octopus reversibly changing skin appearance when flashing its blue rings as a warning display⁶². **B** Pictures of an individual blue ring reversibly switching between hidden (left) and exposed (right) states on a contrast-enhancing brown dermal background⁶². **C** Schematics of the envisioned octopus-inspired deception and signaling systems before (left) and after (right) actuation. The proposed devices consist of a top transparent proton-conducting polymer electrode, a nonacene variant-based active layer wherein a wrinkled blue annulus surrounds a flatter

brown circle, an underlying acrylic dielectric elastomer membrane, and a bottom transparent proton-conducting polymer electrode (top left and top right insets). Before actuation, the devices feature contracted microstructured active regions with bright visible appearances, strong near-infrared signatures, and large fluorescence signals (bottom left), but after actuation, the devices feature expanded nanostructured active regions with light visible appearances, weak near-infrared signatures, and small fluorescence signals (bottom right). The images in panels A and B are adapted from ref. 62 and reproduced with permission from The Company of Biologists Ltd.

nanostructured active regions with lighter visible appearances, weaker associated near-infrared signatures, and smaller corresponding fluorescence signals (Fig. 1C, right). Due to this design strategy, we envisage that the proposed deception and signaling devices will demonstrate functionalities analogous to those of the *H. lunulata* octopus' blue rings and exhibit a highly desirable combination of capabilities and metrics not reported together for any appearance-changing platform to date^{1–11}.

Results

Guided design, facile synthesis, and computational analysis of the nonacene-like molecule

As the active material for our bioinspired platform, we conceived and designed a nonacene-like molecule with a unique architecture by drawing upon literature precedent. In our design, we first started with an extended all-carbon nonacene core, i.e., nine ortho-annulated benzene rings in a linear arrangement, which would furnish a relatively low bandgap and thus a red-to-near-infrared absorbance (Fig. 2A, black)^{33,34}. We next expanded this pi-conjugated core by adding four peripheral fused aromatic rings, which would substantially enhance stability through introduction of multiple aromatic sextets (Fig. 2A, gray)^{53,55}. We in turn incorporated nitrogen heteroatoms within two of the peri-annulated rings, which would afford responsiveness to

chemical stimuli such as protonation (Fig. 2A, blue)^{47,49}. We last included pendant alkyl chain-functionalized phenyl rings near the nitrogens, which would mitigate intramolecular pi-pi stacking and improve solubility in multiple different solvents (Fig. 2A, green)^{31,51}. We theorized that the resulting nonacene-like molecular architecture would feature the spectroscopic properties, ambient-atmosphere stability, and general good solubility essential for demanding camouflage (or other) device applications.

We initially developed a facile strategy for the synthesis of our nonacene-like molecule, which was denoted as tetrabenzononacene or TBN in accordance with prior precedent^{63,64}. For this purpose, we employed modified versions of the literature methodologies established for the preparation and characterization of nitrogen-containing tetrabenzenopentacenes, polyquinolineanthracenes, and zigzag polyquinolines (see sections I.A.1 and I.A.2 in the Supplementary Information)^{63,64,68,69}. In brief, we initially obtained the previously reported 1,5-dichloro-9,10-diethynylanthracene (**1**) precursor and the required didodecyl-substituted phenylmethanimine anthracene (**2**) precursor according to known procedures (see section I.A.2 in the Supplementary Information and Fig. 2B, left)^{63,64,68,69}. We then generated the key dinaphthoquinolineanthracene (**3**) intermediate in reasonable yield by reacting precursors (**1**) and (**2**) via the Lewis acid-mediated aza-Diels–Alder (Povarov) reaction (see section I.A.2 in the

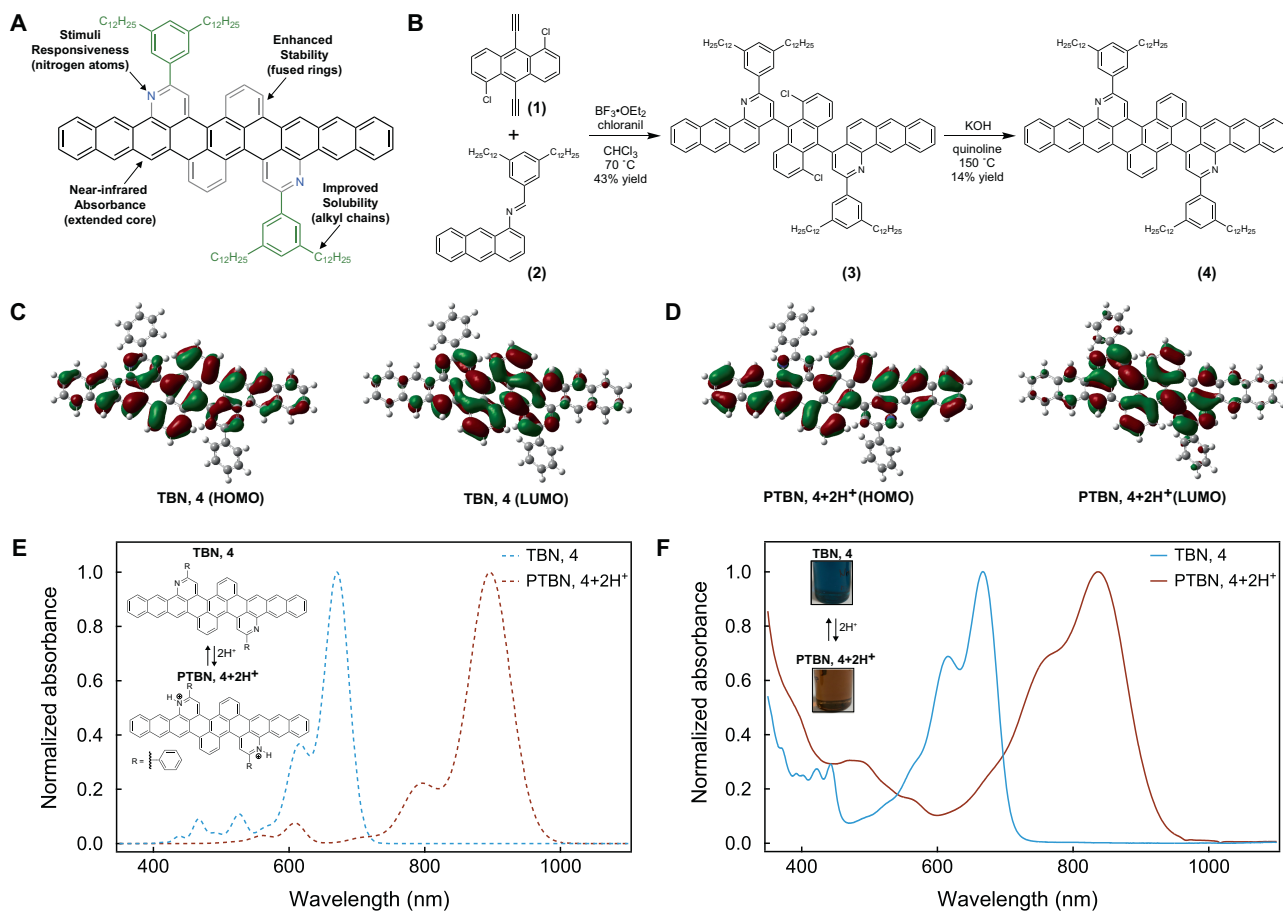


Fig. 2 | Design, synthesis, simulation, and spectroscopy of the nonacene variant. **A** The design of our nonacene-like molecule, where the extended all-carbon nonacene core (black) results in a near-infrared absorbance, the fused peripheral aromatic rings (gray) enhance stability, the nitrogen heteroatoms (blue) introduce stimuli responsiveness, and the pendant alkyl-functionalized phenyl rings (green) improve solubility. **B** The synthetic route for the preparation of nonacene-like molecule **4**, where the two key steps involve a Lewis acid-mediated aza-Diels–Alder reaction and a base-mediated cyclidehydrohalogenation reaction.

C The HOMO (left) and LUMO (right) calculated for the unprotonated tetrabenzononacene TBN, **4**. **D** The HOMO (left) and LUMO (right) calculated for PTBN, **4+2H⁺**. **E** The theoretical UV–Vis–NIR absorption spectra calculated for TBN, **4** (blue dashed line) and PTBN, **4+2H⁺** (brown dashed line). The chemical structures of TBN and PTBN are inset. **F** The experimental UV–Vis–NIR absorption spectra measured for TBN, **4** (blue solid line) and PTBN, **4+2H⁺** (brown solid line). The pictures of the TBN and PTBN solutions in chloroform are inset. Note that the theoretical and experimental absorption spectra were normalized to unity for clarity.

Supplementary Information and Fig. 2B, middle)^{63,64,68,69}. We next converted intermediate (3) into the desired nonacene-like molecule (4) in moderate yield by forming internal C–C bonds between the anthracene core and its two pendant naphthoquinolines via a base-mediated cyclodehydrohalogenation reaction (see section I.A.2 in the Supplementary Information and Fig. 2B, right)⁶³. Here, we characterized precursor (2), intermediate (3), and product (4) via standard methods, i.e., a combination of ¹H NMR spectroscopy, ¹³C NMR spectroscopy, and mass spectrometry (see Supplementary Figs. 1–8 and section I.A.3 in the Supplementary Information). In addition, we further confirmed the identity of product (4) by performing size exclusion chromatography (SEC) for the isolated pure material (Supplementary Fig. 9), simulating the obtained matrix-assisted laser-desorption ionization (MALDI) mass spectrum to confirm the isotopic distribution pattern (Supplementary Figure 10), and collecting 2D ¹H–¹H correlation spectroscopy (COSY) spectra to assign the expected multi-nuclear spin systems (Supplementary Figure 11). Overall, our target compound was synthesized by employing straightforward reaction conditions, isolated in yields reasonable for quantities of tens-to-hundreds of milligrams, and rigorously characterized with a suite of complementary techniques.

We proceeded to obtain computational insight into the likely conformation and electronic properties of our synthesized nonacene-like molecule. Specifically, we calculated the ground-state geometries, electronic structures, and molecular orbitals for both the unprotonated tetrabenazononacene (TBN, 4) and the protonated tetrabenazononacene (PTBN, 4 + 2H⁺) by employing conventional density functional theory (DFT) and unrestricted broken symmetry DFT with the B3LYP functional and the 6-311G (d,p) basis set (note that the side chains were excluded for computational tractability) (see section I.B.1 in the Supplementary Information)^{53–55,63,70–75}. The molecular geometries predicted for TBN and PTBN by using standard DFT revealed twisted concave nonacene cores and downward-oriented tilted phenyl rings, suggesting that solubility would be enhanced due to disruption of intermolecular pi-pi stacking interactions (see Supplementary Data 1 and Supplementary Data 2). The corresponding highest occupied molecular orbitals (HOMOs) and lowest unoccupied molecular orbitals (LUMOs) calculated for TBN and PTBN by using standard DFT featured comparable shapes and nearly encompassed the pi-conjugated cores, albeit with reduced LUMO electron densities at the molecular termini (Fig. 2C, D). Here, the HOMO and LUMO energies were -5.01 eV and -3.11 eV, respectively, for TBN, whereas the HOMO and LUMO energies were -9.59 eV and -8.07 eV, respectively, for PTBN, suggesting enhanced oxidation resistance for the molecule upon protonation^{37–39,44,45,49}. Moreover, the electronic configurations predicted for TBN and PTBN with unrestricted broken symmetry DFT were closed-shell, suggesting reduced reactivity for the molecule with respect to the open-shell all-carbon nonacene (Supplementary Table 1)^{51–58,74,75}. The calculations and analyses together indicated that our designer macromolecule would possess increased solubility in standard solvents and enhanced stability in ambient atmosphere.

We also obtained computational insight into the anticipated optical properties of our synthesized nonacene-like molecule. In particular, we simulated the ultraviolet–visible–near-infrared (UV–Vis–NIR) absorption spectra for TBN and PTBN by employing time-dependent density functional theory (TDDFT) together with the Franck-Condon approximation and evaluated the nature of the associated electronic transitions by leveraging procedures validated for analogous molecular systems (see section I.B.2 in the Supplementary Information)^{72,73,76–81}. For TBN (Fig. 2E, inset), the simulated absorption spectrum revealed an onset at ~725 nm, a main peak at ~670 nm resulting from the first two excited states, a large shoulder at ~632 nm resulting from the vibronic progression of the two lower-energy excited states, and multiple smaller peaks between ~550 nm

and ~420 nm corresponding to the three higher-energy excited states (Fig. 2E, blue and Supplementary Fig. 12). For PTBN (Fig. 2E, inset), the simulated absorption spectrum revealed an onset at ~1000 nm, a main peak at ~896 nm resulting from the two lower-energy excited states, a large shoulder at ~798 nm resulting from the vibronic progression of the first two excited states, and multiple smaller peaks between ~650 nm and ~520 nm corresponding to the three higher-energy excited states (Fig. 2E, brown and Supplementary Fig. 13). Here, the absorption spectrum predicted for PTBN was red-shifted by >200 nm relative to the one predicted for TBN, in agreement with theoretical and experimental precedent for N-heteroacenes^{47,49,72,73}. Interestingly, the bright first excited states and dark second excited states calculated for TBN and PTBN were polarized along and orthogonal to the nonacene core, in contrast to computational findings for the parent all-carbon molecule (Supplementary Table 2)^{80,81}. The simulations and analyses together indicated that our designer macromolecule would absorb light in the red-to-near-infrared regions of the electromagnetic spectrum and that a routine chemical stimulus (protonation) would shift its absorbance further into the near-infrared range.

Solution-phase and solid-state spectroscopic characterization of the nonacene-like molecule

We further advanced our efforts by systematically investigating the electronic and optical properties of our nonacene-like molecule. For this purpose, we prepared TBN solutions by dissolving the compound in organic solvents, converted TBN solutions into PTBN solutions through the addition of acid, and interrogated such solutions with UV–Vis–NIR spectroscopy in ambient atmosphere (see sections I.C.1 and I.C.2 in the Supplementary Information). For TBN solubilized in chloroform, the absorption spectra revealed an onset at ~708 nm, a major peak with a maximum at ~667 nm, and a cluster of sharp small peaks between ~600 nm and ~360 nm (Fig. 2F, blue). Such solutions featured a bright blue color at high molecular concentrations (Fig. 2F, inset). For PTBN solubilized in chloroform, the absorption spectra revealed an onset of ~924 nm, a major peak with a maximum at ~837 nm, and a cluster of broadened small peaks between ~600 nm and ~400 nm (Fig. 2F, brown). Such solutions featured a dark brown color at high molecular concentrations (Fig. 2F, inset). Here, the absorption spectra obtained for PTBN were red-shifted by >170 nm relative to those obtained for TBN, as expected from our theoretical predictions (*vide supra*) and extensive literature precedent for N-heteroacenes^{47,49,72,73}. Moreover, the conversion of TBN into PTBN was dependent on the amount of added acid, reversible with concentrated base, and achievable in multiple solvent/acid systems (Supplementary Figs. 14, 15). Notably, the experimentally obtained spectra were in reasonable agreement with the theoretically predicted spectra, with the differences likely resulting from the limited accuracy of the employed functionals and the influence of challenging-to-simulate solvation effects (compare, for example, Fig. 2E, F and Supplementary Figs. 14, 15)^{82,83}. These spectroscopic measurements demonstrated that our designer macromolecule featured good solubility and proved that protonation could modulate its visible to near-infrared solution absorbance.

We next evaluated the stability of our nonacene-like molecule under conditions that would prove challenging for any acene variant. Towards this end, we prepared solutions containing TBN, PTBN, or 6,13-bis((trimethylsilyl)ethynyl)pentacene (i.e., TMS-pentacene, which is a classic reference compound with well-known improved stability)^{45,84}, and we then comparatively characterized such solutions with UV–Vis–NIR spectroscopy during high-intensity broadband illumination in ambient atmosphere (see section I.C.3 in the Supplementary Information). Under our intentionally harsh conditions, TBN's peak absorbance decayed relatively rapidly with a half-life of 0.3 ± 0.1 minutes, but PTBN's peak absorbance decayed

> 7800-fold more slowly with a half-life of 2358 ± 307 min (Supplementary Fig. 16). By comparison, TMS-pentacene's peak absorbance decayed rapidly with a half-life of 35.2 ± 1.5 min (Supplementary Fig. 16). Therefore, both TBN and PTBN withstood environmental conditions that would instantaneously decompose any of the reported nonacenes (Supplementary Table 1), with PTBN even exhibiting a >65-fold solution-phase stability enhancement relative to the well-known TMS-pentacene reference compound. Remarkably, TBN showed no obvious signs of degradation even after >2 years of storage as a solid or in solution and thus demonstrated a >10-fold stability enhancement relative to the reported nonacene derivatives, as confirmed by UV-Vis-NIR spectroscopy, proton NMR spectroscopy, and MALDI mass spectrometry (see Supplementary Table 1, section I.A.2 in the Supplementary Information, and Supplementary Figs. 7, 11, 17, 18). These measurements showcased our designer macromolecule's outstanding general robustness under extreme conditions and therefore portended favorably for the material's utility in demanding deception and signaling applications.

We in turn studied the solid-state spectroscopic properties of films from highly soluble, exceptionally stable, and readily processable TBN in a device-relevant configuration. To achieve this goal, we fabricated tri-layer architectures for which a dropcast neat TBN film was the

central layer by drawing upon protocols validated for analogous systems^{66,67}, and we characterized these architectures with digital camera imaging (DCI), atomic force microscopy (AFM), and UV-Vis-NIR spectroscopy, both without and with mechanical actuation (see Supplementary Fig. 19A and section I.D in the Supplementary Information). The unactuated TBN-based architectures featured bright blue colorations and microstructured surface topographies (Fig. 3A, top). The corresponding spectra revealed absorptances of $-30.6 \pm 2.6\%$, transmittances of $-63.4 \pm 2.5\%$, and reflectances of $-6.0 \pm 0.1\%$ at ~ 676 nm (Fig. 3A, bottom). The actuated TBN-based architectures featured lighter blue colorations and >2-fold flatter topographies (Fig. 3B, top). The corresponding spectra revealed decreased absorptances of $-11.6 \pm 1.7\%$, increased transmittances of $-81.1 \pm 1.1\%$, and comparable reflectances of $-7.2 \pm 0.6\%$ at ~ 676 nm (Fig. 3B, bottom). Here, our TBN-based architectures' lowered absorptances and enhanced transmittances presumably resulted from strain-induced reductions in both their effective thicknesses and substantial surface roughnesses, in agreement with prior findings^{66,67}. Remarkably, TBN-based architectures fabricated from TBN solutions stored for >2 years featured actuation-dependent visible appearances, surface topologies, and spectroscopic characteristics that were quite similar to those of analogous architectures fabricated from freshly prepared TBN solutions

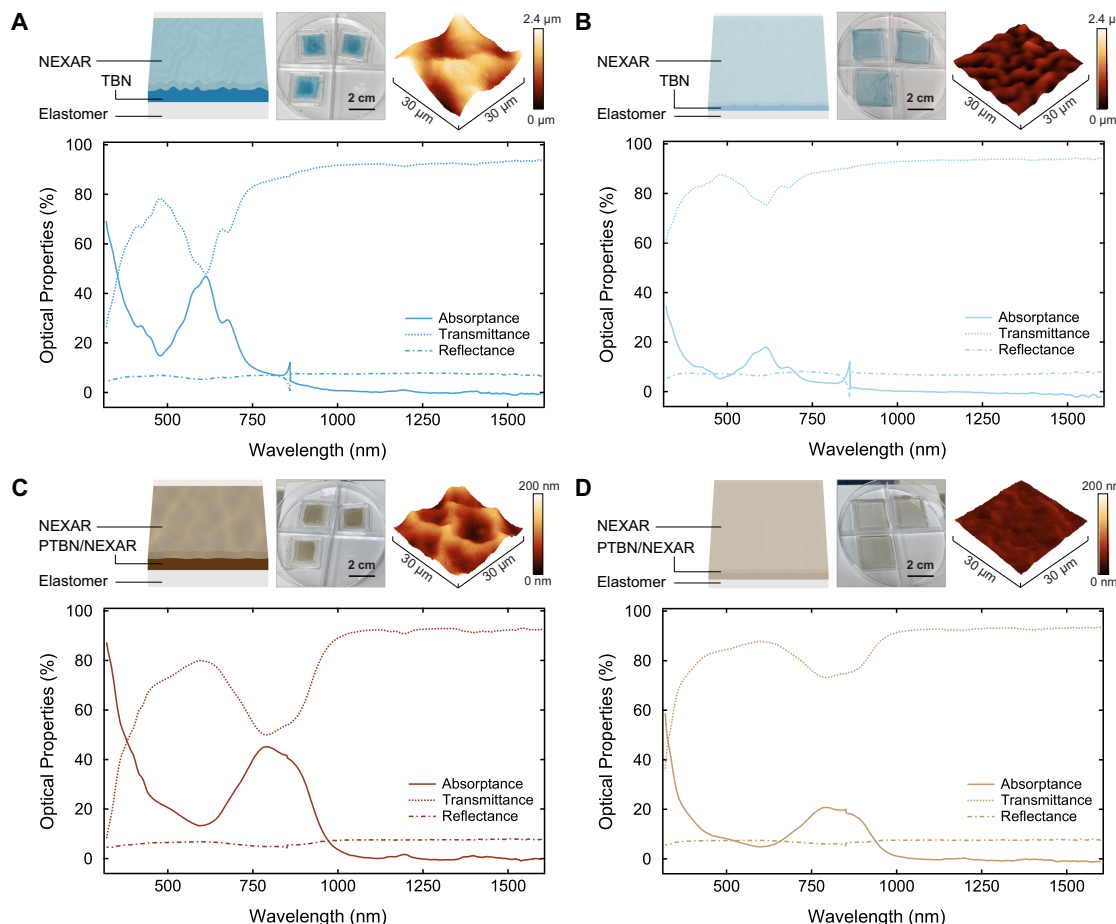


Fig. 3 | Physical and spectroscopic characterization of films from TBN and PTBN in device-relevant configurations. A Top: Schematic (left), pictures (middle), and AFM images (right) of unactuated TBN-based tri-layer architectures. Bottom: Representative UV-Vis-NIR absorptance (dark blue solid line), transmittance (dark blue dotted line), and reflectance (dark blue dashed-dotted line) spectra for unactuated tri-layer TBN-based architectures. **B** Top: Schematic (left), pictures (middle), and AFM images (right) of actuated TBN-based tri-layer architectures. Bottom: Representative UV-Vis-NIR absorptance (light blue solid line), transmittance (light blue dotted line), and reflectance (light blue dashed-dotted line) spectra for actuated TBN-based tri-layer architectures. **C** Top: Schematic (left), pictures (middle), and AFM images (right) of unactuated PTBN-based tri-layer architectures. Bottom: Representative UV-Vis-NIR absorptance (dark brown solid line), transmittance (dark brown dotted line), and reflectance (dark brown dashed-dotted line) spectra for unactuated PTBN-based tri-layer architectures. **D** Top: Schematic (left), pictures (middle), and AFM images (right) of actuated PTBN-based tri-layer architectures. Bottom: Representative UV-Vis-NIR absorptance (light brown solid line), transmittance (light brown dotted line) and reflectance (light brown dashed-dotted line) spectra for actuated PTBN-based tri-layer architectures.

spectra for actuated TBN-based tri-layer architectures. **C** Top: Schematic (left), pictures (middle), and AFM images (right) of unactuated PTBN-based tri-layer architectures. Bottom: Representative UV-Vis-NIR absorptance (dark brown solid line), transmittance (dark brown dotted line), and reflectance (dark brown dashed-dotted line) spectra for unactuated PTBN-based tri-layer architectures. **D** Top: Schematic (left), pictures (middle), and AFM images (right) of actuated PTBN-based tri-layer architectures. Bottom: Representative UV-Vis-NIR absorptance (light brown solid line), transmittance (light brown dotted line) and reflectance (light brown dashed-dotted line) spectra for actuated PTBN-based tri-layer architectures.

(compare Fig. 3A, B and Supplementary Fig. 20). The experiments indicated that our nonacene-like molecule was a suitable active material for the envisioned deception and signaling platforms.

We analogously studied the solid-state spectroscopic properties of films from highly soluble, exceptionally stable, and readily processable PTBN in a device-relevant configuration. To achieve this goal, we fabricated tri-layer architectures for which a dropcast mixed PTBN/NEXAR™ sulfonated pentablock copolymer (NEXAR) film was the central layer by drawing upon protocols validated for analogous systems^{66,67}, and we characterized the architectures with DCI, AFM, and UV–Vis–NIR spectroscopy, both without and with mechanical actuation (see Supplementary Fig. 19B and section I.D in the Supplementary Information). The unactuated PTBN-based architectures featured dark brown colorations and nanostructured surface topographies (Fig. 3C, top). The corresponding spectra revealed absorptances of $-43.7 \pm 1.2\%$, transmittances of $-51.3 \pm 1.1\%$, and reflectances of $-5.0 \pm 0.1\%$ at -792 nm (Fig. 3C, bottom). The actuated PTBN-based architectures featured lighter brown colorations and >3 -fold flatter surface topographies (Fig. 3D, top). The corresponding spectra revealed decreased absorptances of $-21.4 \pm 2.4\%$, increased transmittances of $-72.5 \pm 2.3\%$, and comparable reflectances of $-6.1 \pm 0.2\%$ at -792 nm (Fig. 3D, bottom). Here, our PTBN-based architectures' lowered absorptances and enhanced transmittances presumably resulted primarily from a strain-induced reduction in their effective thicknesses, in agreement with prior findings^{66,67}. The experiments further underscored the suitability of our nonacene-like molecule for applications in the envisioned deception and signaling platforms.

Development and validation of deception and signaling systems from the nonacene-like molecule

We continued our efforts by manufacturing the envisioned octopus blue ring-inspired systems and studying their appearance-changing

functionalities within the visible region of the electromagnetic spectrum. For this purpose, we employed modified and improved versions of methodologies previously established for the preparation of adaptive infrared camouflage platforms with less advanced capabilities^{66,67}. We accordingly fabricated quad-layer dielectric elastomer actuator (DEA) devices for which the active layer consisted of TBN-based blue annulus enclosing a PTBN/NEXAR-based brown circle (see Supplementary Fig. 21 and section I.E.1 in the Supplementary Information). We then visualized and quantified the color lightness and areal strain for such DEA devices via DCI during variable-bias electrical actuation above a white scattering background under standard indoor lighting in ambient atmosphere (see sections I.E.2 and I.E.3 in the Supplementary Information). For our devices, the blue-brown annulated circles simultaneously expanded laterally and became noticeably lighter upon actuation with large biases of either -2.9 kV or -3.2 kV (Supplementary Fig. 22, Fig. 4A, B, and Supplementary Movie 1). The active regions' areal strains and lightness changes featured characteristic dependences on the magnitude of the applied voltage, with average strains of $-79 \pm 6\%$ and $-45 \pm 4\%$ and average lightness changes of $-14 \pm 1\%$ and $-5 \pm 2\%$ for the blue outer annuli and brown inner circles, respectively, at a -3.2 kV bias (Fig. 4C). Moreover, the devices exhibited rapid response times of $\sim 380\text{ msec}$ when repeatedly actuated by a 0.5 Hz frequency square waveform with a 0 kV minimum and a -2.9 kV maximum (Fig. 4D). When considered together, the experiments showed that devices from our nonacene-like molecule featured dynamic visible appearance-changing capabilities and operational performances that compared favorably to those reported for analogous camouflage platforms^{1–11,65–67}.

Having demonstrated the appearance-changing functionalities of our octopus blue ring-inspired systems, we sought to rigorously evaluate their operational stabilities. To achieve this goal, we systematically characterized the color lightness of 10 different quad-layer DEA

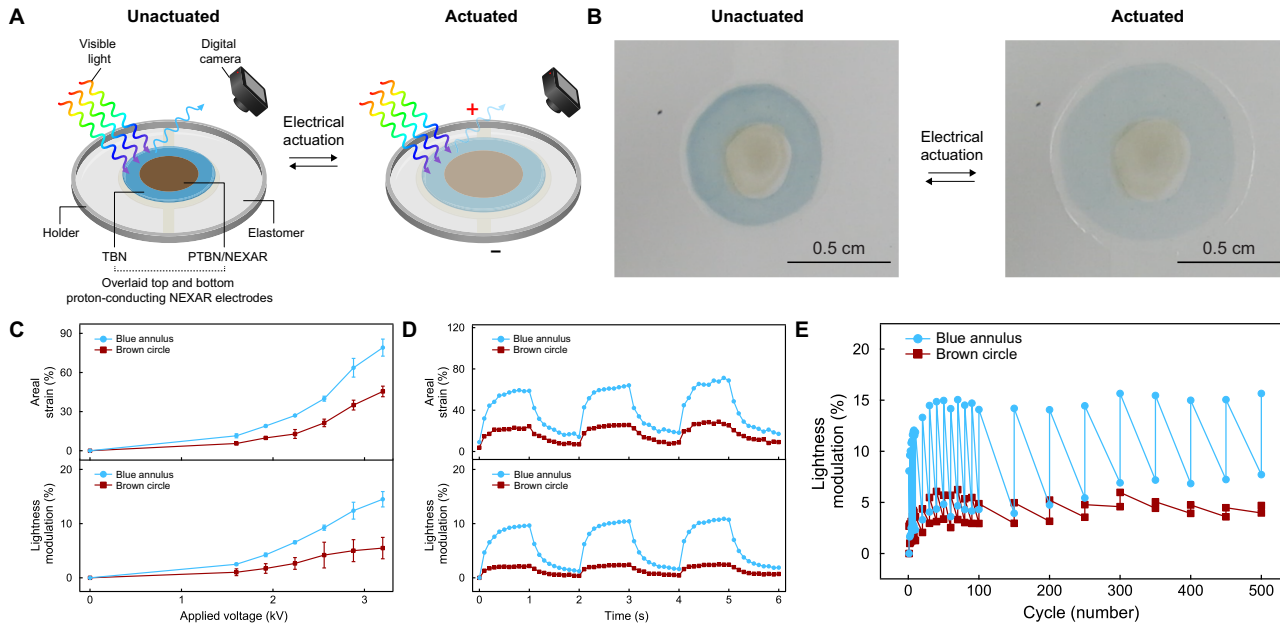


Fig. 4 | Appearance-changing functionalities, operational performances, and cycling stabilities of TBN- and PTBN-based systems. **A** Schematic of a visible appearance-changing system undergoing monitoring during electrical actuation under standard indoor lighting in ambient atmosphere. **B** Representative digital camera images of an appearance-changing device before (left) and after (right) electrical actuation with a bias of -3.2 kV . Note the change in area and color lightness for the blue-brown annulated circle as a result of electrical actuation. **C** Top: Plot of the areal strain as a function of the applied voltage for the devices' outer annuli (blue line) and inner circles (brown line). Bottom: Plot of the lightness

modulation as a function of the applied voltage for the devices' outer annuli (blue line) and inner circles (brown line). The error bars represent standard deviations. **D** Top: Plot of the areal strain as a function of time for a representative device's outer annulus (blue line) and inner circle (brown line) over three consecutive on/off actuation cycles. Bottom: Plot of the lightness modulation as a function of time for a representative device's outer annulus (blue line) and inner circle (brown line) over three consecutive on/off actuation cycles. **E** Plot of the lightness modulation as a function of the actuation cycle number for a representative device's outer annulus (blue line) and inner circle (brown line) over 500 sequential actuation cycles.

devices via DCI during hundreds of rounds of repeated electrical actuation with a -2.9 kV bias, again above a white scattering background under standard indoor lighting in ambient atmosphere (see sections I.E.2 and I.E.3 in the Supplementary Information). For 7 of the 10 devices, the blue-brown annulated circles featured uniform coloration and revealed no obvious evidence of physical delamination or electrochemical degradation (Supplementary Fig. 22). These 7 devices continuously operated with stable lightness modulation over at least 500 cycles (Fig. 4E and Supplementary Table 3). For 3 of the 10 devices, the blue-brown annulated circles initially featured uniform coloration but then acquired localized discoloration suggestive of chemical degradation (Supplementary Fig. 23). These 3 devices continuously operated with stable lightness modulation for ~100 to ~400 cycles, spontaneously failed with a corresponding brief pause in functionality, and resumed operating but with altered lightness modulation for ~50 to ~100 more cycles (Supplementary Fig. 24 and Supplementary Table 3). Here, our devices presumably failed through classical dielectric breakdown and pinhole shorting mechanisms common for dielectric elastomer actuators (and other capacitors) and then likely self-repaired through local conversion of our nonacene-like molecule and/or the acrylic elastomer into an insulating material (see Supplementary Fig. 23)^{85–87}. These experiments highlighted our devices' exceptional ambient atmosphere cycling stabilities and revealed their ability to autonomously self-repair without any user intervention, which is a rare capability among dielectric elastomer actuators^{88,89} and has not been reported for analogous camouflage platforms^{1–11,65–67}.

We subsequently investigated the signature management functionalities of our octopus blue ring-inspired systems within the near-infrared region of the electromagnetic spectrum. Towards this end, we visualized and quantified the near-infrared contrast and areal strain for quad-layer devices via spectrally filtered DCI during electrical actuation above a black absorbing background under near-infrared illumination in ambient atmosphere (see section I.E.4 in the Supplementary Information). For our devices, the annulated circles expanded laterally and decreased in contrast with respect to the surroundings upon actuation with a large bias of -3.2 kV (Fig. 5A, B). The active regions' outer annuli and inner circles featured average areal strains of $-73 \pm 3\%$ and $-46 \pm 2\%$ and average contrast changes of $-27 \pm 3\%$ and $-19 \pm 5\%$, respectively, at a -3.2 kV bias (Fig. 5A, B). The devices moreover

demonstrated robust and consistent near-infrared contrast changes during multiple sequential actuation cycles (Supplementary Movie 2). Here, the contrast switching observed for the TBN-based outer annuli and PTBN-based inner circles presumably resulted primarily from modulation of their surface roughness-induced scattering and near-infrared absorbances (see Fig. 3)^{66,67,90}. These experiments showed that devices from our nonacene-like molecule possess near-infrared deception capabilities, which remain highly valued and sought after in camouflage applications^{1–11,65–67}.

We last investigated the signaling functionalities of our octopus blue ring-inspired systems within the visible to near-infrared regions of the electromagnetic spectrum. Towards this end, we visualized and quantified the fluorescence signal intensity and areal strain for quad-layer devices via DCI during electrical actuation above a white scattering background under ultraviolet illumination in ambient atmosphere (see section I.E.5 in the Supplementary Information). For our devices, the annulated circles expanded laterally and decreased in signal intensity with respect to the surroundings upon actuation with a large bias of -3.2 kV (Fig. 5C, D). The active regions' outer annuli and inner circles featured average areal strains of $-74 \pm 4\%$ and $-43 \pm 4\%$ and average signal intensity changes of $-18 \pm 1\%$ and $-6 \pm 2\%$, respectively, at a -3.2 kV bias (Fig. 5C, D). The devices moreover demonstrated robust and consistent fluorescence signal intensity changes during multiple sequential actuation cycles (Supplementary Movie 3). Here, the TBN-based outer annuli exhibited larger signal intensity switching with respect to the PTBN-based inner circles because TBN featured a much stronger visible to near-infrared fluorescence relative to PTBN under ultraviolet (or other) excitation (see Supplementary Fig. 25). These experiments showed that devices from our nonacene-like molecule not only operate stably but also exhibit desirable multispectral signaling capabilities, even under challenging and deleterious continuous ultraviolet irradiation.

Discussion

In summary, we have reported a readily synthesized, theoretically tractable, highly soluble, and exceptionally stable nonacene-like molecule, and our discoveries represent an exciting advance from an organic materials chemistry perspective for multiple reasons. First, our functionalized and expanded nonacene-like molecule is synthesized

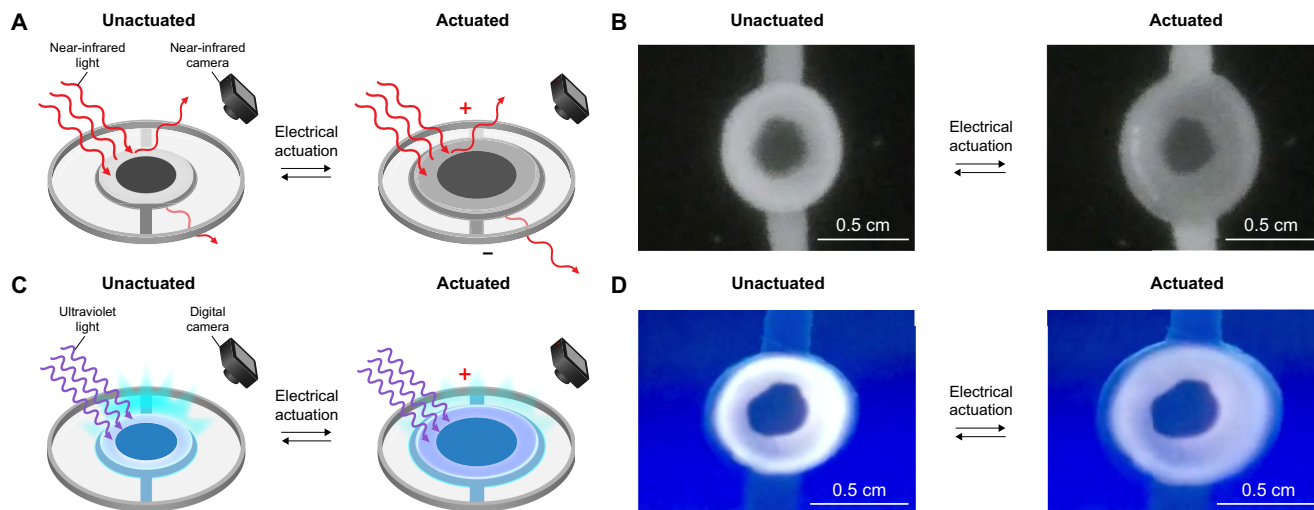


Fig. 5 | Signature management and signaling functionalities of TBN- and PTBN-based systems. **A** Schematic of a near-infrared signature management system undergoing monitoring during electrical actuation under near-infrared illumination in ambient atmosphere. **B** Representative spectrally filtered digital camera images of a signature management device before (left) and after (right) electrical actuation with a bias of -3.2 kV. Note the changes in area and near-infrared contrast

for the annulated circle as a result of electrical actuation. **C** Schematic of a fluorescence signaling system undergoing monitoring during electrical actuation under ultraviolet illumination in ambient atmosphere. **D** Representative digital camera images of a signaling device before (left) and after (right) electrical actuation with a bias of -3.2 kV. Note the changes in area and fluorescence signal intensity for the annulated circle as a result of electrical actuation.

by employing straightforward reaction conditions and in yields reasonable for quantities of tens-to-hundreds of milligrams, thereby adding to the few previously described solution-phase syntheses of comparable large acenes (Supplementary Table 1). Additionally, our nonacene-like molecule features tunable electronic, optical, and physical properties that are inspired by literature precedent and are in good agreement with theoretical predictions (*vide supra*), thus establishing a conceptual framework for the continued engineering and improvement of its highly desirable characteristics. Furthermore, the molecule demonstrates unrivaled and exceptional stability, including the ability to survive direct high-intensity illumination for over a full day when protonated (representing a >65-fold improvement relative to a well-known acene standard) and the ability to withstand solution-phase or solid-state storage for >2 years with no obvious degradation (representing a >10-fold improvement relative to the reported nonacene derivatives) (Supplementary Table 1). Last, the molecule exhibits good solubility at high concentrations in multiple different solvents, presumably due to its twisted aromatic core and pendant alkyl chain-functionalized phenyl rings, and thus can be directly processed into large-area films via standard techniques even after >2 years of storage, which has not been possible for other nonacenes (Supplementary Table 1). Overall, the described designer macromolecule features an outstanding combination of characteristics that objectively improve upon and advance the comparable state-of-the-art acene materials.

We have moreover taken advantage of our nonacene-like molecule's favorable physical properties for the development of multi-functional octopus-inspired deception and signaling systems, and our discoveries are exciting from the perspective of color- and appearance-changing platforms for multiple reasons. First, appearance-changing systems from our nonacene-like molecule are fabricated via routine benchtop techniques using minimal equipment and constitute the only reported integration of a nonacene variant into functional devices of any kind (Supplementary Table 1), thereby reinforcing the exceptional stability and ready processability of our active material. Additionally, the baseline performance of our electro-mechanical systems compares favorably to that reported for analogous camouflage platforms, with figures of merit that include maximum areal strains >-90% and response times of <-400 ms. Furthermore, our actuator-type systems not only consistently and reliably change their visible appearance for ~500 cycles, with minimal-to-no degradation in functionality under ambient conditions, but also unexpectedly possess the ability to autonomously self-repair without user intervention (Supplementary Table 3), which is rare among other dielectric elastomer actuators and not known for analogous camouflage platforms. Last, our systems demonstrate a unique combination of capabilities in the UV–Vis–NIR region of the electromagnetic spectrum, including the ability to modulate visible color lightness, change near-infrared contrast, and adjust multispectral fluorescence intensity. Altogether, our octopus-inspired deception and signaling systems feature a powerful and unique combination of advantages with respect to other camouflage technologies (e.g., straightforward benchtop fabrication, competitive baseline performance metrics, robustness during cycling with the capacity for autonomous self-repair, and multiple dynamic multispectral operating modes)^{1–11,65–67}.

When looking forward, we anticipate that our discoveries will afford a range of promising scientific and technological opportunities for both organic electronic materials and appearance-changing platforms alike. For example, our computationally validated molecular engineering strategy and facile solution-phase synthetic methodology could be extended to the preparation of longer variably functionalized acenes, allowing for the fundamental investigation of these molecules' length-dependent electronic structures and, most critically, anticipated ambient-atmosphere stabilities. In turn, the advantageous photophysical robustness and solution-phase processability of our

nonacene-like molecule and, presumably, of its longer variants, will facilitate future investigation of such materials within the context of traditional optoelectronic systems (e.g., light-emitting diodes, solar cells, and field effect transistors), therefore allowing for the elucidation of extended acenes' theoretically predicted but experimentally elusive superior materials properties for traditional devices. Subsequently, the routine benchtop strategies validated for the fabrication of our octopus-inspired deception and signaling systems, together with the favorable physical properties expected for longer analogous designer acene variants, should enable the scalable manufacturing of devices with even larger areas, as well as the incorporation of additional dynamic modalities for such devices, thereby addressing other grand challenges for all camouflage technologies. Finally, the further detailed exploration of our systems' long-term cyclical stabilities and unexpected autonomous self-repair capabilities may unlock new approaches to understanding and mitigating classical defect-based failure mechanisms for both dielectric elastomer actuators and color- and appearance-changing platforms. Assuming the realization of the described possibilities, the exciting findings reported herein could ultimately influence areas as varied as organic and functional materials, bioinspired and biomimetic photonics, biological and chemical sensing, biomedical imaging and bioelectronics, energy generation and conservation, and soft actuation and robotics.

Methods

The extended details for the Synthesis and Chemical Characterization of the Nonacene-Like Molecule are provided in Section I.A of the Supplementary Information; the extended details for the Computational Analysis of the Nonacene-Like Molecule are provided in Section I.B of the Supplementary Information; the extended details for the Solution-Phase Spectroscopy of the Nonacene-Like Molecule are provided in Section I.C of the Supplementary Information; the extended details for the Fabrication, Mechanical Actuation, and Characterization of the Tri-Layer Architectures from the Nonacene-Like Molecule are provided in Section I.D of the Supplementary Information; and the extended details for the Fabrication, Electrical Actuation, and Characterization of the Quad-Layer Devices from the Nonacene-Like Molecule are provided in Section I.E of the Supplementary Information.

Data availability

All data needed to evaluate the described conclusions are present in the manuscript and/or the supplementary materials. The coordinates of the optimized structures for TBN, **4** and PTBN, **4 + 2H⁺** are provided in the source data files. Other relevant data are available from the authors upon request. Source data are provided with this paper.

References

1. Kolle, M. & Lee, S. Progress and opportunities in soft photonics and biologically inspired optics. *Adv. Mater.* **30**, 1702669 (2018).
2. Isapour, G. & Lattuada, M. Bioinspired stimuli-responsive color-changing systems. *Adv. Mater.* **30**, 1707069 (2018).
3. Ko, J. H., Yoo, Y. J., Lee, Y., Jeong, H. & Song, Y. M. A review of tunable photonics: optically active materials and applications from visible to terahertz. *iScience* **25**, 104727 (2022).
4. Li, Z. & Chen, W. Progress in dynamic emissivity regulation: control methods, material systems, and applications. *Mater. Chem. Front.* **5**, 6315–6332 (2021).
5. Dou, S. et al. Bioinspired microstructured materials for optical and thermal regulation. *Adv. Mater.* **33**, 2000697 (2021).
6. Shao, L., Zhuo, X. & Wang, J. Advanced plasmonic materials for dynamic color display. *Adv. Mater.* **30**, 1704338 (2018).
7. Degenstein, L. M., Sameoto, D., Hogan, J. D., Asad, A. & Dolez, P. I. Smart textiles for visible and IR camouflage application: state-of-

- the-art and microfabrication path forward. *Micromachines* **12**, 773 (2021).
8. Hu, R. et al. Thermal camouflaging metamaterials. *Mater. Today* **45**, 120–141 (2021).
 9. Qiao, Y., Meng, Z., Wang, P. & Yan, D. Research progress of bionic adaptive camouflage materials. *Front. Mater.* **8**, 637664 (2021).
 10. Bu, X. & Bai, H. Recent progress of bio-inspired camouflage materials: from visible to infrared range. *Chem. Res. Chin. Univ.* **39**, 19–29 (2023).
 11. Yang, J. et al. Beyond the visible: bioinspired infrared adaptive materials. *Adv. Mater.* **33**, 2004754 (2021).
 12. Hong, W., Yuan, Z. & Chen, X. Structural color materials for optical anticounterfeiting. *Small* **16**, 1907626 (2020).
 13. Sun, Y., Le, X., Zhou, S. & Chen, T. Recent progress in smart polymeric gel-based information storage for anti-counterfeiting. *Adv. Mater.* **34**, 2201262 (2022).
 14. Tadepalli, S., Slocik, J. M., Gupta, M. K., Naik, R. R. & Singamaneni, S. Bio-optics and bio-inspired optical materials. *Chem. Rev.* **117**, 12705–12763 (2017).
 15. Qin, M., Sun, M., Hua, M. & He, X. Bioinspired structural color sensors based on responsive soft materials. *Curr. Opin. Solid State Mater. Sci.* **23**, 13–27 (2019).
 16. Hong, G., Antaris, A. L. & Dai, H. Near-infrared fluorophores for biomedical imaging. *Nat. Biomed. Eng.* **1**, 0010 (2017).
 17. Lee, G. H. et al. Multifunctional materials for implantable and wearable photonic healthcare devices. *Nat. Rev. Mater.* **5**, 149–165 (2020).
 18. Li, W. & Fan, S. Nanophotonic control of thermal radiation for energy applications. *Opt. Express* **26**, 15995 (2018).
 19. Peng, Y. & Cui, Y. Advanced textiles for personal thermal management and energy. *Joule* **4**, 724–742 (2020).
 20. Liu, T.-Y., Qin, P. & Liu, J. Intelligent liquid integrated functional entity: a basic way to innovate future advanced biomimetic soft robotics. *Adv. Intell. Syst.* **1**, 1900017 (2019).
 21. Xiong, J., Chen, J. & Lee, P. S. Functional fibers and fabrics for soft robotics, wearables, and human–robot interface. *Adv. Mater.* **33**, 2002640 (2021).
 22. Wu, W., Wang, M., Ma, J., Cao, Y. & Deng, Y. Electrochromic metal oxides: recent progress and prospect. *Adv. Electron. Mater.* **4**, 1800185 (2018).
 23. Rai, V., Singh, R. S., Blackwood, D. J. & Zhili, D. A review on recent advances in electrochromic devices: a material approach. *Adv. Eng. Mater.* **22**, 2000082 (2020).
 24. He, Q., Sun, S. & Zhou, L. Tunable/reconfigurable metasurfaces: physics and applications. *Research* **2019**, 1849272 (2019).
 25. Lin, Y. S. & Xu, Z. Reconfigurable metamaterials for optoelectronic applications. *Int. J. Optomechatronics* **14**, 78–93 (2020).
 26. Kamely, N. Interaction of light with different electroactive materials: a review. *J. Electron. Mater.* **51**, 953–965 (2022).
 27. Ren, H. & Wu, S. T. Adaptive lenses based on soft electroactive materials. *Appl. Sci.* **8**, 1085 (2018).
 28. Faustini, M. Sol-gel engineering to tune structural colours. *J. Sol-Gel Sci. Technol.* **95**, 504–516 (2020).
 29. Xiong, R. et al. Biopolymeric photonic structures: design, fabrication, and emerging applications. *Chem. Soc. Rev.* **49**, 983–1031 (2020).
 30. Colusso, E. & Martucci, A. An overview of biopolymer-based nanocomposites for optics and electronics. *J. Mater. Chem. C* **9**, 5578–5593 (2021).
 31. Anthony, J. E. Functionalized acenes and heteroacenes for organic electronics. *Chem. Rev.* **106**, 5028–5048 (2006).
 32. Anthony, J. E. The larger acenes: versatile organic semiconductors. *Angew. Chem. Int. Ed.* **47**, 452–483 (2008).
 33. Bettinger, H. F. Electronic structure of higher acenes and polyacene: the perspective developed by theoretical analyses. *Pure Appl. Chem.* **82**, 905–915 (2010).
 34. Sun, Z. & Wu, J. Higher order acenes and fused acenes with near-infrared absorption and emission. *Aust. J. Chem.* **64**, 519–528 (2011).
 35. Bunz, U. H., Engelhart, J. U., Lindner, B. D. & Schaffroth, M. Large N-heteroacenes: new tricks for very old dogs? *Angew. Chem. Int. Ed.* **52**, 3810–3821 (2013).
 36. Thorley, K. J. & Anthony, J. E. The electronic nature and reactivity of the larger acenes. *Isr. J. Chem.* **54**, 642–649 (2014).
 37. Miao, Q. Ten years of N-heteropentacenes as semiconductors for organic thin-film transistors. *Adv. Mater.* **26**, 5541–5549 (2014).
 38. Miao, Q. *Polycyclic Arenes and Heteroarenes: Synthesis, Properties, and Applications* (John Wiley & Sons, 2015).
 39. Bunz, U. H. The larger linear N-heteroacenes. *Acc. Chem. Res.* **48**, 1676–1686 (2015).
 40. Bettinger, H. F. & Tönshoff, C. The longest acenes. *Chem. Rec.* **15**, 364–369 (2015).
 41. Dorel, R. & Echavarren, A. M. Strategies for the synthesis of higher acenes. *Eur. J. Org. Chem.* **2017**, 14–24 (2017).
 42. Pham, H. D. et al. Acene-based organic semiconductors for organic light-emitting diodes and perovskite solar cells. *J. Mater. Chem. C* **6**, 9017–9029 (2018).
 43. Sung, M. J. et al. Acene-modified small-molecule donors for organic photovoltaics. *Chem. Eur. J.* **25**, 12316–12324 (2019).
 44. Müller, M., Ahrens, L., Brosius, V., Freudenberg, J. & Bunz, U. H. Unusual stabilization of larger acenes and heteroacenes. *J. Mater. Chem. C* **7**, 14011–14034 (2019).
 45. Dong, S., Ong, A. & Chi, C. Photochemistry of various acene based molecules. *J. Photochem. Photobiol. C* **38**, 27–46 (2019).
 46. Chen, W., Yu, F., Xu, Q., Zhou, G. & Zhang, Q. Recent progress in high linearly fused polycyclic conjugated hydrocarbons (PCHs, n>6) with well-defined structures. *Adv. Sci.* **7**, 1903766 (2020).
 47. Brega, V., Yan, Y. & Thomas, S. W. Acenes beyond organic electronics: sensing of singlet oxygen and stimuli-responsive materials. *Org. Biomol. Chem.* **18**, 9191–9209 (2020).
 48. Tönshoff, C. & Bettinger, H. F. Pushing the limits of acene chemistry: the recent surge of large acenes. *Chem. Eur. J.* **27**, 3193–3212 (2021).
 49. Richards, G. J. & Hill, J. P. The pyrazinacenes. *Acc. Chem. Res.* **54**, 3228–3240 (2021).
 50. Yunus, Y. et al. Review of the common deposition methods of thin-film pentacene, its derivatives, and their performance. *Polymers* **14**, 1112 (2022).
 51. Kaur, I., Jazdzky, M., Stein, N. N., Prusevich, P. & Miller, G. P. Design, synthesis, and characterization of a persistent nonacene derivative. *J. Am. Chem. Soc.* **132**, 1261–1263 (2010).
 52. Purushothaman, B., Bruzek, M., Parkin, S. R., Miller, A. F. & Anthony, J. E. Synthesis and structural characterization of crystalline nonacenes. *Angew. Chem. Int. Ed.* **50**, 7013–7017 (2011).
 53. Xiao, J. et al. Synthesis and structure characterization of a stable nonatwistacene. *Angew. Chem. Int. Ed.* **51**, 6094–6098 (2012).
 54. Wang, Y. et al. Synthesis and characterization of oxygen-embedded quinoidal pentacene and nonacene. *J. Am. Chem. Soc.* **141**, 2169–2176 (2019).
 55. Müller, M. et al. Tetrabenzonononacene: “butterfly wings” stabilize the core. *Angew. Chem.* **132**, 1982–1985 (2020).
 56. Yang, X., Rominger, F. & Mastalerz, M. Benzo-fused perylene oligomers with up to 13 linearly annulated rings. *Angew. Chem. Int. Ed.* **60**, 7941–7946 (2021).
 57. Jančářík, A., Holec, J., Nagata, Y., Šámal, M. & Gourdon, A. Preparative-scale synthesis of nonacene. *Nat. Commun.* **13**, 223 (2022).

58. Tönshoff, C. & Bettinger, H. F. Photogeneration of octacene and nonacene. *Angew. Chem. Int. Ed.* **49**, 4125–4128 (2010).
59. Zuzak, R. et al. Nonacene generated by on-surface dehydrogenation. *ACS Nano* **11**, 9321–9329 (2017).
60. Urgel, J. I. et al. On-surface light-induced generation of higher acenes and elucidation of their open-shell character. *Nat. Commun.* **10**, 861 (2019).
61. Ayani, C. G. et al. Efficient photogeneration of nonacene on nanostructured graphene. *Nanoscale Horiz.* **6**, 744–750 (2021).
62. Mathger, L. M., Bell, G. R. R., Kuzirian, A. M., Allen, J. J. & Hanlon, R. T. How does the blue-ringed octopus (*Hapalochlaena lunulata*) flash its blue rings? *J. Exp. Biol.* **215**, 3752–3757 (2012).
63. Park, Y. S. et al. Synthesis of nitrogen-containing rubicene and tetrabenzopentacene derivatives. *Angew. Chem.* **128**, 3413–3416 (2016).
64. Feng, Z. et al. Bottom-up synthesis of nitrogen-containing graphene nanoribbons from the tetrabenzopentacene molecular motif. *Carbon* **170**, 677–684 (2020).
65. Xu, C., Stuibianu, G. T. & Gorodetsky, A. A. Adaptive infrared-reflecting systems inspired by cephalopods. *Science* **359**, 1495–1500 (2018).
66. Xu, C., Colorado Escobar, M. & Gorodetsky, A. A. Stretchable cephalopod-inspired multimodal camouflage systems. *Adv. Mater.* **32**, 1905717 (2020).
67. Liu, Y., Feng, Z., Xu, C., Chatterjee, A. & Gorodetsky, A. A. Reconfigurable micro-and nano-structured camouflage surfaces inspired by cephalopods. *ACS Nano* **15**, 17299–17309 (2021).
68. Dibble, D. J. et al. Aza-diels-alder approach to diquinolineanthracene and polydiquinolineanthracene derivatives. *Org. Lett.* **20**, 502–505 (2018).
69. Umerani, M. J. et al. Synthesis of polyquinolines via an AA/BB-type aza-diels-alder polymerization reaction. *J. Mater. Chem. C* **4**, 4060–4066 (2016).
70. Becke, A. D. Density-functional thermochemistry. III. The role of exact exchange. *J. Chem. Phys.* **98**, 5648–5652 (1993).
71. Lee, C., Yang, W. & Parr, R. G. Development of the Colle-Salvetti correlation-energy formula into a functional of the electron density. *Phys. Rev. B* **37**, 785–789 (1988).
72. Fleischhauer, J. et al. A way to stable, highly emissive fluorubine dyes: tuning the electronic properties of azaderivatives of pentacene by introducing substituted pyrazines. *Chem. Eur. J.* **18**, 4549–4557 (2012).
73. Richards, G. J. et al. Amphiprotism-coupled near-infrared emission in extended pyrazinacenes containing seven linearly fused pyrazine units. *J. Am. Chem. Soc.* **141**, 19570–19574 (2019).
74. Bendikov, M. et al. Oligoacenes: theoretical prediction of open-shell singlet diradical ground states. *J. Am. Chem. Soc.* **126**, 7416–7417 (2004).
75. Yang, Y., Davidson, E. R. & Yang, W. Nature of ground and electronic excited states of higher acenes. *Proc. Natl. Acad. Sci. USA* **113**, 5098–5107 (2016).
76. Imrota, R., Barone, V. & Santoro, F. Ab initio calculations of absorption spectra of large molecules in solution: Coumarin C153. *Angew. Chem. Int. Ed.* **46**, 405–408 (2007).
77. Santoro, F., Imrota, R., Lami, A., Bloino, J. & Barone, V. Effective method to compute Franck-Condon integrals for optical spectra of large molecules in solution. *J. Chem. Phys.* **126**, 084509 (2007).
78. Muniz-Miranda, F. et al. Benchmarking TD-DFT against vibrationally resolved absorption spectra at room temperature: 7-aminocoumarins as test cases. *J. Chem. Theory Comput.* **11**, 5371–5384 (2015).
79. Mukazhanova, A. et al. Accurate first-principles calculation of the vibronic spectrum of stacked perylene tetracarboxylic acid diimides. *J. Phys. Chem. A* **124**, 3055–3063 (2020).
80. Chakraborty, H. & Shukla, A. Pariser-Pople model based investigation of ground and low-lying excited states of long acenes. *J. Phys. Chem. A* **117**, 14220–14229 (2013).
81. Bettinger, H. F., Tonshoff, C., Doerr, M. & Sanchez-Garcia, E. Electronically excited states of higher acenes up to nonacene: a density functional theory/multireference configuration interaction study. *J. Chem. Theory Comput.* **12**, 305–312 (2016).
82. Laurent, A. D. & Jacquemin, D. TD-DFT benchmarks: a review. *Int. J. Quant. Chem.* **113**, 2019–2039 (2013).
83. Ali, A. et al. TD-DFT benchmark for UV-visible spectra of fused-ring electron acceptors using global and range-separated hybrids. *Phys. Chem. Chem. Phys.* **22**, 7864–7874 (2020).
84. Maliakal, A., Raghavachari, K., Katz, H., Chandross, E. & Siegrist, T. Photochemical stability of pentacene and a substituted pentacene in solution and in thin films. *Chem. Mater.* **16**, 4980–4986 (2004).
85. Vaicekauskate, J., Yu, L. & Skov, A. L. Insights into the complex prebreakdown actuation of silicone elastomers and its influence on breakdown behavior. *ACS Omega* **5**, 18584–18593 (2020).
86. Carpi, F. *Dielectric Elastomers as Electromechanical Transducers: Fundamentals, Materials, Devices, Models and Applications of an Emerging Electroactive Polymer Technology* (Elsevier Science, 2008).
87. Peline, R. & Kornbluh, R. Dielectric Elastomers as Electroactive Polymers (EAPs): Fundamentals. in *Electromechanically Active Polymers* (ed. Carpi, F.) 671–686 (Springer, 2016).
88. Yuan, W. et al. Fault-tolerant dielectric elastomer actuators using single-walled carbon nanotube electrodes. *Adv. Mater.* **20**, 621–625 (2008).
89. Stoyanov, H. et al. Long lifetime, fault-tolerant freestanding actuators based on a silicone dielectric elastomer and self-clearing carbon nanotube compliant electrodes. *RSC Adv.* **3**, 2272–2278 (2013).
90. Mangold, K., Shaw, J. A. & Vollmer, M. The physics of near-infrared photography. *Eur. J. Phys.* **34**, S51–S71 (2013).

Acknowledgements

The authors thank Dr. Irina Gorodetskaya and Dr. Aleiza Farrukh for their invaluable discussions, and the authors also thank Ms. Melissa Sung for assistance with the figure graphics. The authors acknowledge financial support from the Defense Advanced Research Projects Agency (cooperative agreements W911NF-16-2-0077 and D16AP00034 to A.A.G.), the Office of Naval Research (grants N00014-17-1-2564 and N00014-21-1-2143 to A.A.G.), and the National Science Foundation (grant DMR-1847774 to S.S.). The authors thank the Laser Spectroscopy Laboratories (LSL) at the University of California, Irvine, the Nuclear Magnetic Resonance (NMR) Spectroscopy Facility at the University of California, Irvine, the Mass Spectrometry Facility at the University of California, Irvine, and the Massachusetts Green High-Performance Computing Center (MGHPCC) for the use of their equipment and resources.

Author contributions

A.A.G. conceived and designed the experiments. D.J.D., A.M.B., R.K., R.L., and P.R.D. synthesized and characterized the compounds. P.P., C.X., D.J.D., and R.K. performed the solution-phase spectroscopy experiments. C.X. fabricated and characterized the electrically actuated devices. A.M. and S.S. performed the theoretical calculations and simulations. C.X. and P.L. fabricated and characterized the mechanically actuated architectures. P.P., C.X., D.J.D., P.L., and A.M.B. analyzed and interpreted the experimental data. A.M. and S.S. analyzed and interpreted the theoretical data. P.P., C.X., D.J.D., P.L., A.M.B., and A.A.G. prepared the figures and wrote the manuscript. All authors contributed to the Supplementary Information.

Competing interests

The authors have submitted an invention disclosure to the University of California, Irvine that describes the design and working principles of the reported octopus-inspired deception and signaling systems.

Additional information

Supplementary information The online version contains supplementary material available at
<https://doi.org/10.1038/s41467-023-40163-7>.

Correspondence and requests for materials should be addressed to Alon A. Gorodetsky.

Peer review information *Nature Communications* thanks Felix Plasser and the other, anonymous, reviewer(s) for their contribution to the peer review of this work.

Reprints and permissions information is available at
<http://www.nature.com/reprints>

Publisher's note Springer Nature remains neutral with regard to jurisdictional claims in published maps and institutional affiliations.

Open Access This article is licensed under a Creative Commons Attribution 4.0 International License, which permits use, sharing, adaptation, distribution and reproduction in any medium or format, as long as you give appropriate credit to the original author(s) and the source, provide a link to the Creative Commons license, and indicate if changes were made. The images or other third party material in this article are included in the article's Creative Commons license, unless indicated otherwise in a credit line to the material. If material is not included in the article's Creative Commons license and your intended use is not permitted by statutory regulation or exceeds the permitted use, you will need to obtain permission directly from the copyright holder. To view a copy of this license, visit <http://creativecommons.org/licenses/by/4.0/>.

© The Author(s) 2023